JOURNAL OF SYNCHROTRON RADIATION
ISSN 1600-5775

Repeatability and sensitivity characterization of the far-field high-energy diffraction microscopy instrument at the Advanced Photon Source

Jun-Sang Park,* Hemant Sharma and Peter Kenesei

Advanced Photon Source, Argonne National Laboratory, Lemont, IL 60439, USA.
*Correspondence e-mail: parkjs@anl.gov

Received 25 February 2021
Accepted 11 August 2021

Edited by V. Favre-Nicolin, ESRF and Université Grenoble Alpes, France

Keywords: far-field high-energy diffraction microscopy; FF-HEDM; 3DXRD; measurement sensitivity.

In the last two decades, far-field high-energy diffraction microscopy (FF-HEDM) and similar non-destructive techniques have been actively developed at synchrotron light sources around the world. As these techniques (and associated analysis tools) are becoming more available for the general users of these light sources, it is important and timely to characterize their performance and capabilities. In this work, the FF-HEDM instrument implemented at the 1-ID-E endstation of the Advanced Photon Source (APS) is summarized. The set of measurements conducted to characterize the instrument's repeatability and sensitivity to changes in grain orientation and position are also described. When an appropriate grain matching method is used, the FF-HEDM instrument's repeatability is approximately 5 μm in translation, 0.02° in rotation, and 2×10^{-4} in strain; the instrument sensitivity is approximately 5 μm in translation and 0.05° in rotation.

1. Introduction

The ability to non-destructively map the internal structure of polycrystalline materials has made significant progress in the past two decades. In particular, experimental techniques that utilize high-energy X-rays to obtain crystallographic orientation and strain tensor maps of a polycrystalline material in its bulk form have made great strides. This class of experimental techniques combined with appropriate analysis strategies is capable of delivering these maps with varying degrees of resolution, precision, and accuracy. Some examples of these experimental techniques include high-energy diffraction microscopy (HEDM) or three-dimensional X-ray diffraction (3DXRD) (Poulsen *et al.*, 2001; Suter *et al.*, 2006; Lienert *et al.*, 2011), diffraction contrast tomography (Ludwig *et al.*, 2009), and diffraction aperture X-ray microscopy (Larson *et al.*, 2004).

At the 1-ID beamline of the Advanced Photon Source (APS), Argonne National Laboratory, several variants of HEDM are used to investigate a wide variety of material systems, often *in situ* (Lienert *et al.*, 2011; Park *et al.*, 2015; Bernier *et al.*, 2020). Based largely on these developments, a new high-throughput HEDM instrument is being commissioned at the 6-ID-D endstation of the APS (Sagoff, 2020), and the High Energy X-ray Microscope beamline with performance exceeding that of the 1-ID beamline is planned as a part of the APS upgrade (Fenner, 2021). The purpose of this work is to highlight the salient features of the Far-Field (FF) HEDM instrument and characterize its performance. The performance is characterized using two metrics – repeatability and sensitivity – using a well controlled set of experiments and polycrystalline samples fabricated from materials at nominally

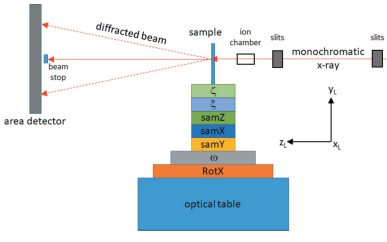

stress-free state. As a high-level overview, the instrument's repeatability is quantified through a set of repeated measurements conducted over a period of time; its sensitivity is quantified through a set of known intentional motions. These will be elaborated on further in the subsequent sections. For the purposes of this work, we define the FF-HEDM instrument as the physical setup that exists at the 1-ID-E endstation combined with the data analysis software suite, namely *Microstructural Imaging using Diffraction Analysis Software* (*MIDAS*), developed at the APS for analyzing different variants of HEDM data (Sharma, 2020).

The paper is organized as follows. The physical setup for FF-HEDM at the 1-ID-E endstation and the *MIDAS* framework used to analyze the FF-HEDM data are described in §2. The sample and the experiment parameters are summarized in §3. This is followed by a description of the analysis method to quantify the instrument's sensitivity in §4 and §5. The results are presented in §6 and are discussed in §7. Finally, we close with a summary and outlook in §8.

2. Description of the instrument

In a typical FF-HEDM experiment, a polycrystalline aggregate is rotated with respect to the incident monochromated high-energy X-rays while a set of diffraction patterns are acquired using an area detector placed downstream of the sample. These patterns consist of diffraction spots from the crystallographic planes of the constituent crystals that satisfy the Bragg diffraction condition as the aggregate is rotated. These spots are extracted from the raw diffraction patterns through image processing using conventional peak fitting or through artificial intelligence and machine learning (Liu *et al.*, 2020) and indexed to obtain the crystallographic orientations, positions, and strains of the constituent grains in the polycrystalline aggregate (Poulsen, 2004). The physical setup of the FF-HEDM instrument is illustrated in §2.1. The coordinate system and associated software framework used to reduce the FF-HEDM data are summarized in §2.2.

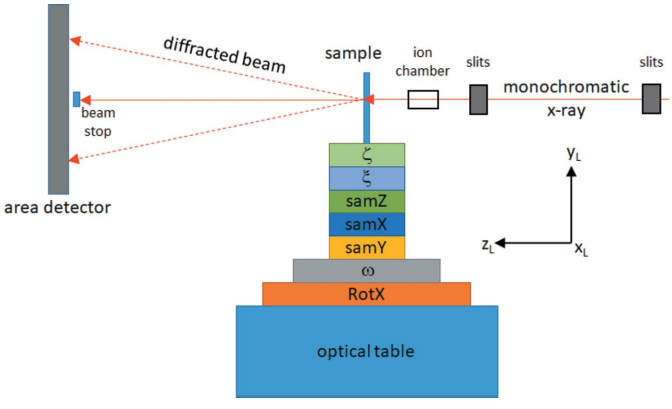

Figure 1
A schematic of the APS 1-ID-E setup for HEDM.

2.1. Physical setup at the 1-ID-E endstation

The FF-HEDM setup is illustrated in Figure 1. The monochromated high-energy X-ray beam is produced from a combination of a superconducting undulator source (Ivanyushenkov *et al.*, 2017) and a bent double Laue high-energy monochromator (Shastri *et al.*, 2002) located approximately 70 m upstream of the endstation. The energy bandwidth of the monochromated beam is approximately 1×10^{-3}. The size of the beam impinging on the sample's volume of interest (VOI) is defined by a series of slits, sometimes in combination with focusing optics (Said & Shastri, 2010; Shastri *et al.*, 2020).[1] Between the final slits and the sample, an ion chamber exists to measure the incident beam flux; its reading is denoted as IC0 hereon. The stage stack illustrated in Figure 1 is assembled to align the rotation stage to the incident beam and the sample to the rotation axis. Table 1 summarizes the available motions, their functions, and motion performance.[2] The motion resolution and repeatability of the hardware used in this work exceed the intentional motions executed. The distance from the top of the rotation stage to the beam is approximately 300 mm and the distance from the top of the optical table to the beam is approximately 700 mm. The optical table is equipped with an inclinometer capable of measuring rotations about $\mathbf{x}_L$ and $\mathbf{z}_L$[3] to monitor the angular perturbation of the table. The area detector is placed approximately 1000 mm from the sample on a separate, stable optical table. The area detector used in this work is an amorphous Si detector with a nominal pixel pitch of 200 µm × 200 µm and detection area of 409.6 mm × 409.6 mm (Lee *et al.*, 2007, 2008). The direct beam is blocked by a beam stop placed in front of the area detector. It consists of a tungsten block with an embedded pin diode often used to acquire transmission information and placed approximately 5 cm in front of the area detector along $\mathbf{z}_L$. The temperature fluctuation in the endstation is approximately ±0.2°C when the endstation remains closed for an extended period of time similar in length as the duration of the measurements conducted for this work.

2.2. *MIDAS* framework for FF-HEDM

There are several software packages available for the analysis of FF-HEDM data (Gotz *et al.*, 2003; Bernier *et al.*, 2011; Schmidt, 2014; Sharma, 2020). In this work, we employ the *MIDAS* software suite for data analysis. Figure 2 illustrates the relevant coordinate systems used in *MIDAS*. Here, a high-

[1] In this work, the sample cross-section width is smaller than the width of the beam; the VOI is always in an illuminated state by the incident X-ray beam. For the case where the samples cross-section is larger than the width of the beam, more advanced techniques inspired by stitching tomography or wide field-of-view tomography (Kyrieleis *et al.*, 2009) or isolating a smaller volume of material using diffracted beam apertures (Gill *et al.*, 2012; Park *et al.*, 2013) can be used for FF-HEDM (Beaudoin *et al.*, 2013).
[2] The intent here is to provide the motion performance information for the individual components that constitute the experimental setup and we do not endorse a particular manufacturer or hardware. Hence, the names of the manufacturers and the part numbers are not provided but they can be shared upon request.
[3] Here, the subscript L denotes the laboratory frame. The laboratory frame is described in §2.2 where we describe the *MIDAS* framework.

Table 1
A summary of the motions available in the stage stack illustrated in Figure 1.

Motion name	Function	Remarks
Optical table	Vertical motion and limited tilts of the entire stack above the table about the nominal $\mathbf{x}_L$ and $\mathbf{z}_L$	Equipped with tilt sensors for stability monitoring; the vertical stages can be manipulated independently to change the angle between $\mathbf{y}_L$ and the sample tomographic rotation axis
RotX	Translation of the rotation stage along the nominal $\mathbf{x}_L$ direction to align the rotation stage with respect to the incident X-ray	Typically equipped with an encoder for repeatability and stability monitoring
ω	Sample tomographic rotation synchronized with the area detector to acquire FF-HEDM data	The accuracy and repeatability are well below 0.001°, based on high-resolution encoder; the axis run-out is well below 1 μm
samY	Sample vertical motion to select the VOI along the length of the sample	The motion accuracy, repeatability, and stability are below 1 μm
samX and samZ	Two horizontal motions to align the sample and the VOI with respect to the rotation stage	The motion accuracy, repeatability, and stability are all below 1 μm
ξ and ζ	Two angular motions to align the sample and the VOI with respect to the incident X-ray	The motion accuracy, repeatability, and stability are all approximately 0.001°

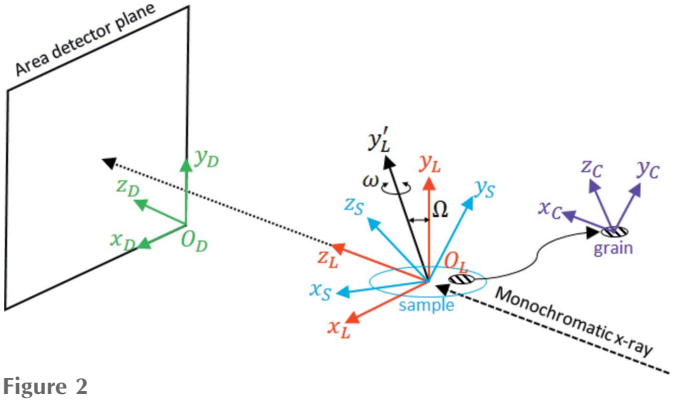

Figure 2
The *MIDAS* analysis framework and relevant coordinate systems. A polycrystalline sample is rotated about $\mathbf{y}'_L$ and the rotation is denoted as ω. The angle between $\mathbf{y}_L$ and $\mathbf{y}'_L$ is denoted as Ω.

level summary of the framework is described. A more detailed description of the framework is presented by Sharma *et al.* (2012*a*,*b*; Sharma, 2021). In Figure 2, the subscripts L, D, S, and C correspond to the laboratory frame, the detector frame, the sample frame, and the crystal frame, respectively. The $\mathbf{z}_L$ direction is the beam propagation direction. Rotation of the sample occurs about $\mathbf{y}'_L$ and it is denoted as ω. For FF-HEDM[4] it is desirable to have $\mathbf{y}'_L$ parallel to $\mathbf{y}_L$[5]; the angle between $\mathbf{y}_L$ and $\mathbf{y}'_L$, denoted as Ω, is defined as the wedge angle. Finally, $\mathbf{x}_L$ is the cross product between $\mathbf{y}_L$ and $\mathbf{z}_L$. The origin of $\mathbf{x}_L$-$\mathbf{y}_L$–$\mathbf{z}_L$ is denoted as $\mathbf{O}_L$. In practice, the vertical blades of the slits are aligned to the $\mathbf{x}_L$–$\mathbf{z}_L$ plane; similarly, when sawtooth refractive lenses are employed (Said & Shastri, 2010; Shastri *et al.*, 2020), the vertically focused planar beam is aligned to the $\mathbf{x}_L$–$\mathbf{z}_L$ plane.

Often, the detector frame does not coincide with the laboratory frame by a simple translation. The goal of detector calibration is to determine the relationship between the two frames and, hence, the location of any point on the area detector with respect to the laboratory frame. Several standards are used for calibration. The nominal distance from $\mathbf{O}_L$ to the detector[6], location of the direct beam on the detector, detector tilt with respect to $\mathbf{x}_L$ and $\mathbf{y}_L$, and the distortion of the detector are determined using the diffraction patterns from CeO_2 (Kaiser & Watters, 2007) or LaB_6 (Freiman & Trahey, 2000). The distortion of the detector is described using a model that combines the approaches presented by Lee *et al.* (2008) and Borbély *et al.* (2014*a*,*b*). These parameters are fine-tuned and the tilt of the detector with respect to $\mathbf{z}_L$ is determined using a ruby (Freiman, 2001) or gold single crystal (Shade *et al.*, 2016) whose lattice parameter and geometry are well known.

The VOI is rotated about $\mathbf{y}'_L$ continuously over a 360° range while area detector patterns are collected at fixed ω intervals. An area detector pattern contains the diffraction spots from the crystallographic planes in the VOI that satisfy the diffraction condition over the ω interval. These diffraction spots and corresponding scattering vectors ($\mathbf{q}$) combined with the nominal crystallographic symmetry and lattice parameters for the material of interest in the VOI are used to determine the center of mass (COM) of the illuminated coherent lattice[7] with respect to $\mathbf{O}_L$; the relationship between the crystal frame and the laboratory frame, commonly referred to as crystallographic orientation, and the elastic strain tensor of each crystal with respect to the prescribed reference state are also determined.

For the amorphous Si detector used in this work, the readout is occurring cyclically row-by-row from the center line of the detector toward the edges in 126 ms with a 124 μs dead-time per each pixel (Lee *et al.*, 2008). Therefore, the dead-time is often negligible relative to the integration time (>150 ms) used in the present study and is not anticipated to influence the measured intensities. However, this also means that the pixels that are closer to and the pixels farther away from the center line of the detector in a frame have slightly different ω

[4] This is also the case for other variants of HEDM at the APS.
[5] It is worthwhile noting that $\mathbf{y}'_L$ is not necessarily orthogonal to $\mathbf{z}_L$ but there exists $\mathbf{y}_L$ that resides in the plane defined by $\mathbf{y}'_L$ and $\mathbf{z}_L$ that is orthogonal to $\mathbf{z}_L$.
[6] This is often referred to as the sample-to-detector distance since the sample is typically placed at $\mathbf{O}_L$ for measurement.
[7] An illuminated coherent lattice will be referred to as a grain hereon.

Table 2
A summary of the FF-HEDM measurements to characterize the instrument's performance.

Dataset label	Motion	Magnitudes	Energy (keV)	Sample-to-detector distance (mm)	Beam size (H × V) (mm)	Remarks
A-SS	–	–	71.68	754	1.6 × 0.2	VOI positioned at $\mathbf{O}_L$; scan repeated 10 times in positive and negative rotation directions over several hours to understand the instrument's stability
B-SS	samX, samZ (μm)	0, 5, 10, 50, 100, 250, 500	65.35	856	1.6 × 0.1 at 65.35 keV	VOI initially positioned at $\mathbf{O}_L$ and translated with respect to $\mathbf{O}_L$; when $\omega = 0°$, samX and samZ moves the sample along $\mathbf{x}_L$ and $\mathbf{z}_L$, respectively
C-SS	ξ (°)	0.00, 0.05 0.10, 0.25, 0.50, 1.00	65.35	856	1.6 × 0.1	Measurement using stainless steel sample; VOI *not* realigned to $\mathbf{O}_L$ after each ξ motion.
C-Au	ξ (°)	0.00, 0.01, 0.05, 0.10, 0.25, 0.50, 1.00	71.68	1093	0.20 × 0.05	Measurement using gold cube sample; VOI positioned at $\mathbf{O}_L$ after each ξ motion using the radiography detector
D-SS	Ω (°)	0.00, −0.25, −0.51	65.35	856	1.6 × 0.1	VOI positioned at $\mathbf{O}_L$ after each Ω motion using the radiography detector

positions. Therefore, a correction for this systematic temporal artifact is to be applied during data processing. Such correction is taken into account in *MIDAS* by considering the appropriate integration interval for each pixel row when calculating the center of mass position of individual diffraction peaks (Sharma, 2021).

It is noteworthy that the relationship between the sample and laboratory frames[8] is not introduced to this framework explicitly; the relationship between the laboratory and sample frames needs to be established through other means such as radiography, tomography, and/or attaching particles to the VOI that are insensitive to the applied stimulus (Shade *et al.*, 2016) so that rigid-body rotation and translation of the VOI can be tracked during an *in situ* experiment or *ex situ* measurements in between which the sample is processed.

3. Instrument performance characterization measurements

A series of measurements were conducted to quantify the FF-HEDM instrument's performance. These consist of the following.

(i) Repeatability – repeated FF-HEDM measurements on an identical VOI to understand the long-term stability and repeatability of the instrument.

(ii) Sensitivity – FF-HEDM measurements with intentional and known sample translation and rotation to understand the smallest translation and rotation magnitudes that the instrument can detect.[9]

(iii) FF-HEDM measurements with the physical setup perturbed from its ideal configuration to understand the perturbation's impact on the resulting microstructure map.

While these are related to the instrument's resolution, precision, and accuracy, we do not employ these terms here because the real microstructure of the VOI interrogated is unknown and the HEDM map and associated quantities rely on a complex workflow that consist of image processing and optimization across the reciprocal and real spaces.

Two samples were employed in this work and they are listed below:

(i) Well annealed austenitic stainless steel (SS) rod with a 1 mm × 1 mm square cross-section. The average grain size of the material is approximately 50 μm. The material is nominally free of preferred crystallographic orientation. A section of the rod was illuminated and measured using X-rays.

(ii) Well annealed gold cube sample with a nominal dimension of 30 μm × 30 μm × 30 μm fabricated as described by Shade *et al.* (2016) and mounted on a platform. This cube nominally consists of two to five grains depending on how the cube is illuminated and data analyzed. In this work, the entire sample was illuminated by X-rays.

Table 2 summarizes the measurements conducted. Dataset A using SS (DS-A-SS) characterizes the *repeatability and stability* of the instrument. Dataset B using SS (DS-B-SS) measures the *translational sensitivity* of the instrument. Dataset C measures the *angular sensitivity* of the instrument using the stainless steel (DS-C-SS) and gold cube (DS-C-Au) samples. Finally, Dataset D using SS (DS-D-SS) explores the *effect of* Ω on the microstructure map acquired using FF-HEDM. As the samples are fabricated from well annealed materials, the strain tensors are anticipated to be small.[10]

In all our measurements, the angular step size is 0.25° yielding 1440 diffraction patterns per FF-HEDM dataset.[11] The energy of the monochromatic X-rays and the nominal sample-to-detector distance are listed in Table 2.[12] The ener-

[8] The sample frame is defined as one that is inherent to the sample from its prior processing history or geometry.

[9] Here, we use the term sensitivity because the microstructure information from an FF-HEDM instrument such as grain center of mass, crystallographic orientation, and strain tensor are derived quantities from detected diffraction spots' motions with respect to a reference position.

[10] We are in the process of fabricating samples and designing an experimental program to quantify the repeatability and sensitivity of the FF-HEDM instrument when the samples are under load.

[11] The exposure time per frame was 0.02 s for most of the measurements with the exception of DS-A-SS (0.3 s).

[12] Here, only a representative subset of a larger dataset acquired at different settings is presented for brevity. The full dataset (raw diffraction patterns and microstructure maps) is available at https://doi.org/10.18126/u4zn-6xzt through the Materials Data Facility (Blaiszik *et al.*, 2016, 2019).

gies of the monochromated X-rays were chosen based on the X-ray absorption-edge energies – the Re *K*-edge is at 71.68 keV and the Hf *K*-edge is at 65.35 keV (Thompson *et al.*, 1985). In between scans, the X-ray energy was monitored by inserting an Re or Hf foil in the beam path. The energy stability of the monochromator employed in this work was approximately ±5 eV. Additional information on the performance of the monochromator has been given by Shastri *et al.* (2002). These measurements were performed at different points in time spanning over a four-year period[13]; the VOI interrogated were also different between the datasets acquired using the stainless stess sample. While conducting these measurements during a single session using identical instrument settings and VOIs would be more desirable, these sets of data indirectly illustrate the instrument's enduring performance over a wide range of settings that can be employed for different material systems and scientific questions.

For all datasets, the sample was initially aligned using samX, samY, samZ, ξ, and ζ such that the center of mass of the stainless steel sample cross-section or the Au sample coincides with $\mathbf{O}_L$. A FF-HEDM dataset was collected here to serve as the reference. Then, the the sample was intentionally moved with respect to $\mathbf{O}_L$ using the specified motion and an FF-HEDM dataset was acquired. Table 2 lists the intentional motions executed. Three types of intentional motions were executed. With the samX and samZ translations, the sample was moved with respect to $\mathbf{O}_L$ in the $\mathbf{x}_L$–$\mathbf{z}_L$ plane to determine the instrument's sensitivity to translation. With the ξ rotation, the sample was tipped to determine the instrument's angular sensitivity. Finally, the rotation axis was intentionally tipped about $\mathbf{x}_L$ such that Ω is no longer zero to understand its effect on the FF-HEDM analysis.

For each motion type and dataset, the goal was to illuminate the same VOI. In the case of samX and samZ translations (DS-B-SS), illuminating the same VOI consistently is a trivial case with the exception of larger motion magnitudes where the periphery of the VOI can move out of the incident beam during the FF-HEDM scan. For DS-C-SS and DS-C-Au where the ξ motion is used, illuminating the same VOI consistently is more challenging because the motion does not necessarily pivot about $\mathbf{O}_L$. This means that a VOI aligned to the beam and established with respect to the laboratory frame when $\xi = 0^\circ$ will not remain at $\mathbf{O}_L$ when $\xi \neq 0^\circ$; it will also move (predominantly) in $\mathbf{y}_L$ when the ξ motion is executed. Similarly, in DS-D-SS where the FF-HEDM instrument is perturbed to accomplish the Ω, the VOI will not pivot about $\mathbf{O}_L$. These unintentional motions can be compensated largely by the samY motion and minor adjustments in samX and samZ motions.[14] All alignment operations were conducted using a radiography detector with a nominal pixel size of 1.2 μm.

4. Data analysis using the *MIDAS* framework

The instrument was initially calibrated using diffraction patterns from CeO_2 or LaB_6 powder. The calibration was refined using a set of FF-HEDM patterns from the annealed polycrystalline gold sample. After calibration, the relationship between the laboratory and the detector frames is fully known. Given this calibration, the FF-HEDM dataset from the material of interest is analyzed using the following workflow.

(i) The analysis starts by identifying all the pixels in each frame that satisfy the lower and upper intensity thresholds. In this work, the lower threshold was determined by visual inspection of the raw diffraction patterns and set just above the detector noise level. The upper threshold was set to 16000 counts.[15]

(ii) These pixels are appropriately merged across the $\mathbf{x}_D$, $\mathbf{y}_D$, and ω as diffraction spots. The diffraction spots are fit for sub-pixel resolution to generate a list of associated scattering vectors, $\mathbf{q}$s.

(iii) Given the list of $\mathbf{q}$s and the nominal lattice parameter and space group of the constituent crystals in the VOI, a candidate list of crystallographic orientations that will satisfy the diffraction condition at those $\mathbf{q}$s are obtained.

(iv) Given the list of $\mathbf{q}$s and the candidate list of orientations, the centers of mass, orientations, and the elastic strain tensors of the crystals are refined iteratively.

For indexing, the completeness (Poulsen *et al.*, 2001) requirement was 0.8, which means that at least 80% of the anticipated diffraction spots need to be detected for a grain and associated orientation, center of mass, equivalent sphere grain radius[16], and strain. The equivalent sphere grain radius is referred to as grain radius or grain size hereon. Unlike near-field HEDM (Suter *et al.*, 2006), we do not obtain a volume-filling orientation map in FF-HEDM; only the COM of the constituent grains and associated mean orientation and the grain-averaged elastic strain tensor are obtained. In this work, each dataset is treated independently; the list of grains obtained from the reference dataset is not used to instantiate the analysis of other datasets. Table 3 lists the crystallographic planes used in the analysis.

5. Grain matching

To determine the FF-HEDM instrument's spatial and angular sensitivity, the list of grains obtained from the intentional motions need to be compared with the reference measurement and the grains need to be matched. In DS-B-SS, for example, the reference grain list (L0) is acquired with the VOI aligned

[13] This was due to the limited beam time availability at the APS 1-ID-E endstation.

[14] This still does not strictly enforce that the volume illuminated by the X-rays when $\xi = 0^\circ$ and $\Omega = 0^\circ$ is identical to the illuminated volume when ξ or Ω are not zero. However, with large sample grain size and relatively small magnitudes of ξ and Ω employed in this work, the effect of these differences on the grain maps is small.

[15] The maximum pixel intensity of the detector is 16383 (2^{14}).

[16] The equivalent sphere radius of a particular grain is estimated by the intensity of the diffraction spots associated with the grain with respect to the total intensity of the FF-HEDM scan (Sharma *et al.*, 2012*a*,*b*).

Table 3
MIDAS analysis parameters used in this work.

Dataset label	Crystallographic planes used	Lower intensity threshold	Anticipated number of diffraction spots per grain	Remarks
A-SS	{220}, {311}, {222}, {400}, {331}, {240}, {422}	50	244	{111} and {200} rings were masked during the data acquisition
B-SS	{111}, {200}, {220}, {311}, {222}, {400}	50	128	–
C-SS	{220}, {311}, {222}, {400}	100	100	–
D-SS	{220}, {311}, {222}, {400}	100	100	Same detector as the one used for dataset C-SS
C-Au	{111}, {200}, {220}, {311}, {222}, {400}	40	128	–

Table 4
A synthetic misorientation table between two sets of grain maps, L0 and L1.

	L0-gr1	L0-gr2	L0-gr3	L0-gr4
L1-gr1	0.93	0.94	0.85	0.99
L1-gr2	0.30	0.21	0.21	0.04
L1-gr3	0.51	0.50	0.76	0.24
L1-gr4	0.88	0.22	0.78	0.33
L1-gr5	0.54	0.84	0.91	0.76
L1-gr6	0.71	0.34	0.56	0.05
L1-gr7	0.72	0.49	0.49	0.62
L1-gr8	0.12	0.99	0.24	0.83

to $\mathbf{O}_L$ and $\mathbf{x}_L$–$\mathbf{y}_L$–$\mathbf{z}_L$. With subsequent intentional translation, a new list of grains is acquired (L1) and L1 is compared with L0.

In the case where there is a small number of grains (DS-C-Au, for instance), each with reasonably unique orientation and position, matching grains between L0 and L1 is relatively trivial. When there are many grains, the matching procedure's design can significantly affect the result; matched grains can be path-dependent. We illustrate this in the following example. Table 4 shows a table of synthetic misorientation angles between the grains in found in L0 and L1.[17] Three matching approaches are considered as listed below.

(i) Matching Method I (MM-I) starts the search from the first grain in L0 (L0-g1) and finds the grain pairs in L1 for all the grains in L0 with the sequence of pair search defined by the grain number in L0.

(ii) MM-II starts the search from the third grain in L0 (L0-g3) and finds the grain pairs in L1 for all the grains in L0; the sequence of pair search was defined by the grain number in L0.

(iii) MM-III considers the entire misorientation table and looks for the grain pair between L0 and L1 that yields the minimum misorientation. The search path is *not* determined by the arbitrary grain number but based on the values that exist in the misorientation table.

The resulting grain pairs determined from the three matching methods are summarized in Table 5. The grain pair results using the three matching methods are different. MM-I and MM-II show that matching results can be order-dependent affected by where the search begins and in what order the search is executed. Therefore, we build on MM-III to compare the lists of grains from intentional motions (Table 2).

Table 5
The grain pairs based on Table 4 using different matching methods.

MM-I	MM-II	MM-III
L0-gr1 → L1-gr8	L0-gr3 → L1-gr2	L0-gr4 → L1-gr2
L0-gr2 → L1-gr2	L0-gr4 → L1-gr6	L0-gr1 → L1-gr8
L0-gr3 → L1-gr7	L0-gr1 → L1-gr8	L0-gr2 → L1-gr4
L0-gr4 → L1-gr6	L0-gr2 → L1-gr4	L0-gr3 → L1-gr7

We consider two tables derived from L0 and L1 – misorientation table using the grain orientations and distance table using the grain COMs. The misorientation table is generated using a Matlab library – OdfPf (https://anisotropy.mae.cornell.edu/onr/Matlab/matlab-functions.html). The distance table is generated using the Euclidean distance definition. Because these tables are in two different units, a unitless misorientation table is generated by dividing the misorientation table by 0.25° and a unitless distance table is generated by dividing the distance table by 200 µm; 0.25° is the scanning step size and 200 µm is the pixel size of the amorphous Si detector used for FF-HEDM scans. Finally, these unitless tables are added to generate the separation table that combines the angular and Euclidean distances between the grains in L0 and L1. The separation table is used with MM-III to find the candidate matching grain pairs. Finally, the candidate grain pairs are filtered using the grain radius information. The radius difference of the candidate-pair grains has to be less than 5% to be declared a pair. The magnitude of the grain radius filter was established by DS-A-SS (§6.1) and used throughout this work.

It is noteworthy that the *MIDAS* grain lists were used as-is for the grain matching operation. This means that the information in the misorientation and distance tables is a convolution of the intentional rigid-body motion and instrumental sensitivity and repeatability (particularly for DS-B-SS, DS-C-SS, DS-D-SS, and DS-C-Au where intentional rigid body motions were used). Furthermore, the median, mean, and/or standard deviation figures presented (§6) are also convolutions of the intentional rigid-body motion and instrumental sensitivity and repeatability. However, because the magnitude of the applied rigid-body motion is known in each case and DS-A-SS establishes the instrument's repeatability, the sensitivity of the instrument can be deduced.

[17] The misorientation values in this table are for illustration purposes only and, therefore, are in arbitrary units. Smaller numbers indicate smaller misorientation and larger numbers indicate larger misorientation. In practice, these values typically take the units for angles and larger values may not indicate larger misorientation when the crystal symmetry is considered.

Table 6
A summary of the repeated measurements (DS-A-SS).

Scan number	N_{grain}	Δ_{SPOT} (%)	Δ_{IC0} (%)
1	214	–	–
2	215	0.67	0.13
3	217	0.63	0.02
4	212	0.66	0.02
5	210	0.54	0.11
6	215	0.53	0.06
7	216	0.74	0.13
8	214	0.66	−0.28
9	212	0.23	−1.69
10	212	−0.38	−1.16

Table 7
A summary of the change in COM and crystallographic orientation during the repeated scan.

	Change in COM along $\mathbf{x}_L$ (μm)	Change in COM along $\mathbf{y}_L$ (μm)	Change in COM along $\mathbf{z}_L$ (μm)	Change in orientation (°)
Mean	−3	1	−1	0.40
Median	−1	1	1	0.01
Standard deviation	38	35	10	3.18

6. Results

6.1. Repeated measurements (DS-A-SS)

For DS-A-SS, ten FF-HEDM scans were performed while the sample was rotated in the positive direction (from −180° to +180°) and another ten scans in the negative rotation direction (Table 2) spanning over several hours. Here, we only show the results from the positive rotation scans for brevity; the findings from the negative rotation scans are consistent and repeatable as those from the positive rotation scans. Table 6 shows the number of grains found (N_{grain}) from the repeated scans. It also shows the %-change in the number of diffraction spots detected (Δ_{SPOT}) and %-change in the IC0 value (Δ_{IC0}) with respect to the first scan. In the first scan, the total number of diffraction spots found was 89515 and the IC0 value was 233.9 kHz. Average N_{grain} is 214 with a standard deviation of 2, maximum of 216 and minimum of 210. During these repeated measurements, Δ_{SPOT} and Δ_{IC0} showed minimal changes. Furthermore, Δ_{SPOT} and Δ_{IC0} did not indicate a strong correlation with the number of found grains.

The grains found in each scan are matched with respect to the grains found from scan 1 using the matching method summarized in §5 *without the volume filter*. The mean, median, and standard deviation of the change in COM along $\mathbf{x}_L$, $\mathbf{y}_L$, $\mathbf{z}_L$, and orientation of the matched grains are computed over the ten scans. Table 7 lists these calculated values. This table shows that the instrument is in general stable and repeatable as indicated by the mean and the median values. However, a large standard deviation indicates that there may be some outlier grains that may be improperly paired.

Table 8 summarizes the number of grains matched for each scan with different grain radius filter levels. The number of grains matched decreases with smaller radius filter. Using 2% radius tolerance, the number of grains from scan 1 that are successfully matched is on average 207 grains out of 214 grains found in scan 1. Table 8 also show that using a bigger radius tolerance allows more grains from two scans to be matched.

Table 8
Number of grains matched with various radius tolerances ranging from 2% to 10%.

In scan 1, 214 grains were found.

Scan number	2% radius filter	5% radius filter	10% radius filter
2	209	210	211
3	205	211	212
4	209	211	211
5	208	213	214
6	206	211	212
7	207	211	211
8	207	212	212
9	205	210	212
10	203	211	211

Table 9
A summary of the change in COM and crystallographic orientation during the repeated scans with the grain volume filter employed.

	Change in COM along $\mathbf{x}_L$ (μm)	Change in COM along $\mathbf{y}_L$ (μm)	Change in COM along $\mathbf{z}_L$ (μm)	Change in orientation (°)
Mean	0	1	−1	0.01
Median	−1	1	−1	0.01
Standard deviation	4	4	3	0.01

Using the matched grain pairs that satisfy the 5% grain radius tolerance, the values presented in Table 7 are recomputed (Table 9). In this case, the difference in COM along $\mathbf{x}_L$, $\mathbf{y}_L$, and $\mathbf{z}_L$ are all on the order of 1 μm with significantly smaller standard deviation than those shown in Table 7. The difference in crystallographic orientation is 0.01° with a small standard deviation. This is because the false positive grain pairs are removed by the grain radius tolerance. The missing grains plotted in orientation space or in physical space did not show any significant trends in those spaces. Figure 3 shows the histograms of change in COM Y without and with the volume filter for one of the scans in the repeatability dataset. Figure 4 shows the histograms of misorientation without and with the volume filter for one of the scans in the repeatability dataset. Both figures show that large outliers are removed through the volume filter.

The radius of the missing grains was in general less than 50 μm while the mean and the standard deviation of the grain radius in the VOI were 61 μm and 13 μm, respectively. This indicates that the missing grains are some of the smaller ones in the VOI. This is further illustrated in Fig. 5. In this figure, the left-hand scatter plot compares the radii of the matched grains obtained at the reference scan (scan 0) and the *N*th scan with the volume filter turned off, and the right-hand scatter plot shows similar data with the volume filter turned on. In both scatter plots, the dotted red line shows the case where the radii of the matched grains are identical. The left-hand figure

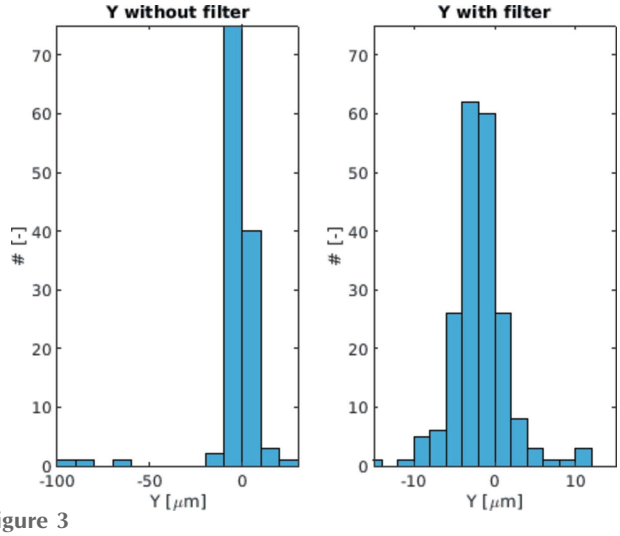

Figure 3
Histograms of COM Y difference between matched grains without (left) and with (right) the volume filter for a repeatability scan. In the left-hand figure, the *Y*-axis is truncated from 120 to show the values at higher *Y* values.

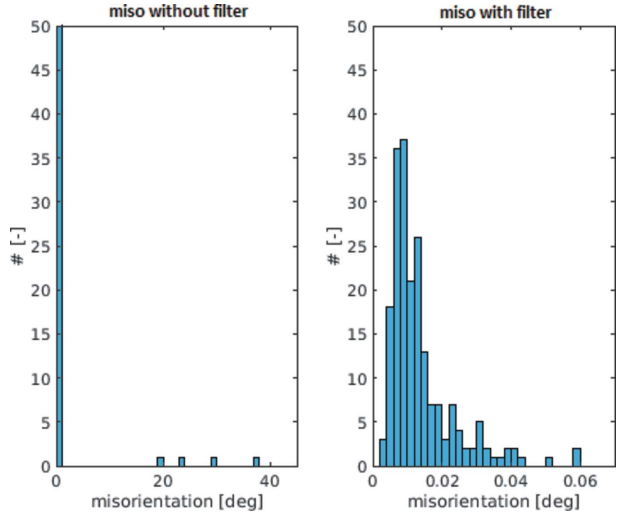

Figure 4
Histograms of misorientation angle between matched grains without (left) and with (right) the volume filter for a repeatability scan. In the left-hand figure, the *Y*-axis is truncated from 170 to show the values at higher misorientation angles.

shows that the grains with significantly different sizes can still be declared as matching when the volume filter is not used; the dots that appear away from the dotted red line illustrate this point.

In the subsequent sections with intentional motions, the grain matching procedure with 5% grain size filter was used, resulting in removing false positive matches and a similar reduction in standard deviation illustrated in Tables 7 and 9.

Figure 6 shows the difference in elastic strain tensors between the tracked grains between the first scan and the third scan (chosen arbitrarily; the other scans also show a similar distribution). This figure shows that for the tracked grains the component-wise difference in strain is negligible on average. However, the difference can be as large as 2×10^{-4}. Table 10

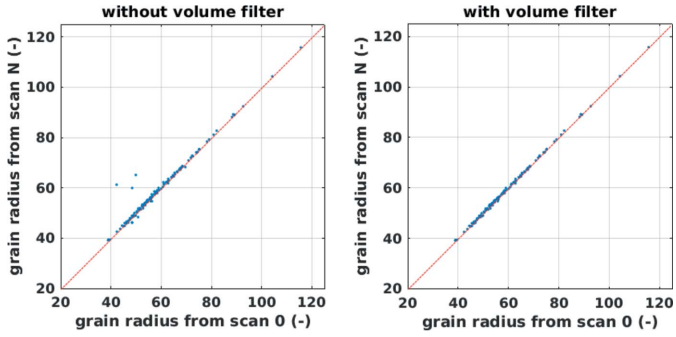

Figure 5
Scatter plots comparing the radii of the matched grains obtained at scan 0 and the *N*th scan. The left-hand plot is without the volume filter and the right-hand plot is with the volume filter used in the grain matching process. The red line is added to show the ideal case where the radii of the matched grains are identical.

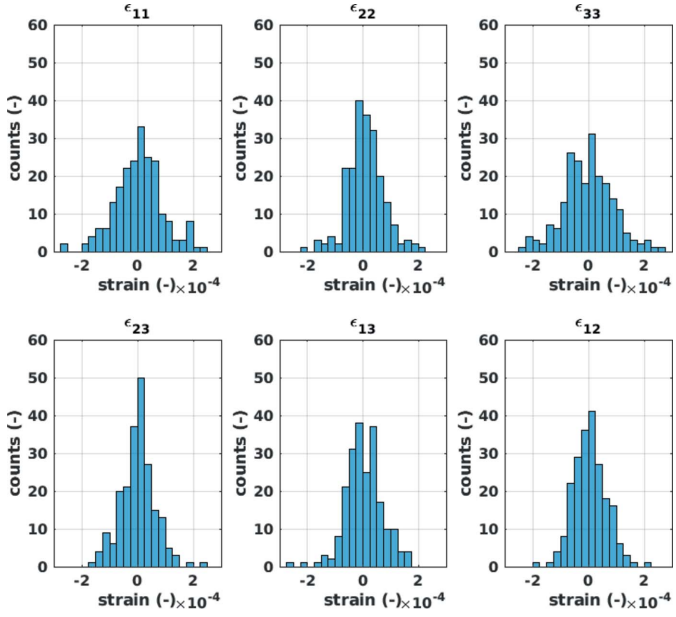

Figure 6
A histogram plot of the change in elastic strain tensors between the tracked grains in DS-A-SS between the first scan and the third scan.

shows the difference in elastic strain tensor over the entire DS-A-SS. Consistent with Fig. 6, the average differences are smaller than 1×10^{-4} but the standard deviation can be as large, 1×10^{-4}. Reducing this distribution will be critical as we push to employ FF-HEDM to investigate rare-event-driven material behavior such as fatigue and crack initiation.

Table 10
A summary of the change in elastic strain during the repeated scan with grain volume filter.

Units in 1×10^{-4} strain.

	ϵ_{11}	ϵ_{22}	ϵ_{33}	ϵ_{23}	ϵ_{13}	ϵ_{12}
Mean	0.14	0.06	0.03	0.02	−0.01	0.04
Median	0.16	0.07	0.09	−0.00	0.01	0.03
Standard deviation	0.99	0.78	1.03	0.65	0.69	0.62

Table 11
A summary of detected motions when the VOI is translated using samX.

The reference scan found 379 grains in the VOI.

Motion using samX (μm)	Median change in COM along $\mathbf{x}_L$ (μm)	Median change in COM along $\mathbf{z}_L$ (μm)	Median change in COM along $\mathbf{y}_L$ (μm)	Median misorientation (°)	Number of grains matched
5	5	0	0	0.03	378
10	9	0	0	0.03	374
50	51	0	−1	0.04	371
100	101	0	0	0.05	353
250	251	0	−1	0.05	350
500	510	0	0	0.06	253

6.2. Intentional translations (DS-B-SS)

For DS-B-SS, the VOI was translated intentionally from $\mathbf{O}_L$ using samX and samZ translations before acquiring FF-HEDM data. Here, only the results from intentional samX motion are presented for brevity; the results from intentional samZ motion and compound samX–samZ motion were similar. Table 11 summarizes the result. The number of grains found in the reference configuration is 379. In general, when the magnitude of intentional motion is less than 50 μm, most of the grains can be mapped back to the grains found in the reference state; for example, with 5 μm intentional translation, 378 out of 379 grains from the reference state are detected. The missing grains are in general small and their orientations and COMs did not show any systematic trends. With larger intentional motions, the number of the grains found and matched to the reference configuration decreases. At 500 μm intentional motion, only 253 grains out of 379 grains found in the reference configuration can be found. The missing grains are located primarily in the periphery of the VOI where the grains are not always illuminated by the incident X-rays.

The median change in COM along $\mathbf{x}_L$ listed in Table 11 is a convolution of the rigid-body motion introduced by the the intentional motion, unintentional motion, and the instrument sensitivity. If the known rigid-body translation component is removed from the median change in COM along $\mathbf{x}_L$, the resulting difference is comparable with the repeatability values associated with DS-A-SS (Table 9) particularly when the magnitude of the intentional motion is small. This implies that the instrument is capable of detecting translation as small as 5 μm, reliably. However, the intentional translation may also be introducing a slight rigid-body rotation as the median misorientation values are slightly larger than those in Table 9. These results indicate that the FF-HEDM instrument is sensitive to approximately 5 μm translation.

Figures 7 and 8 show the differences in strain as the VOI is intentionally translated by 5 μm and 500 μm, respectively. Similar to the DS-A-SS case, the average component-wise strain difference is close to zero but the difference can be as large as 2×10^{-4}. For larger intentional translation (Fig. 8), the standard deviation of the difference distribution is slightly larger. But overall, the strain difference is similar to that observed in DS-A-SS. This implies that smaller rigid-body translations do not affect the strain significantly and the

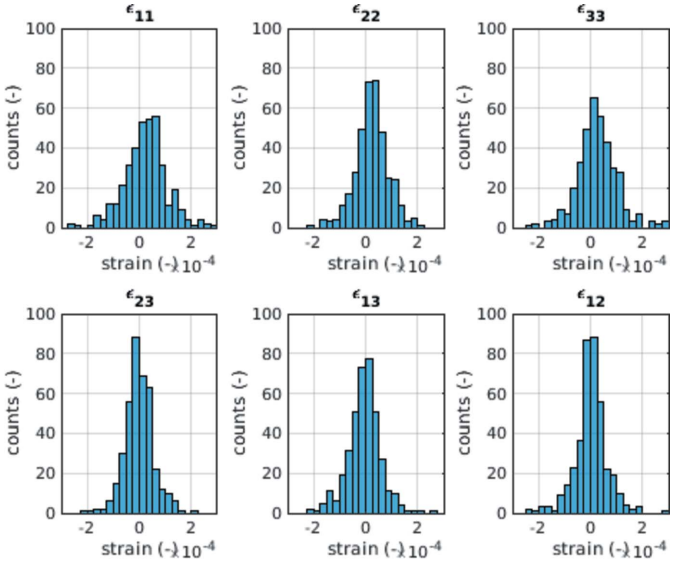

Figure 7
A histogram plot of the difference in elastic strain tensors between the tracked grains in DS-B-SS between the first scan and the scan after 5 μm intentional motion. Strain units in 10^{-4}.

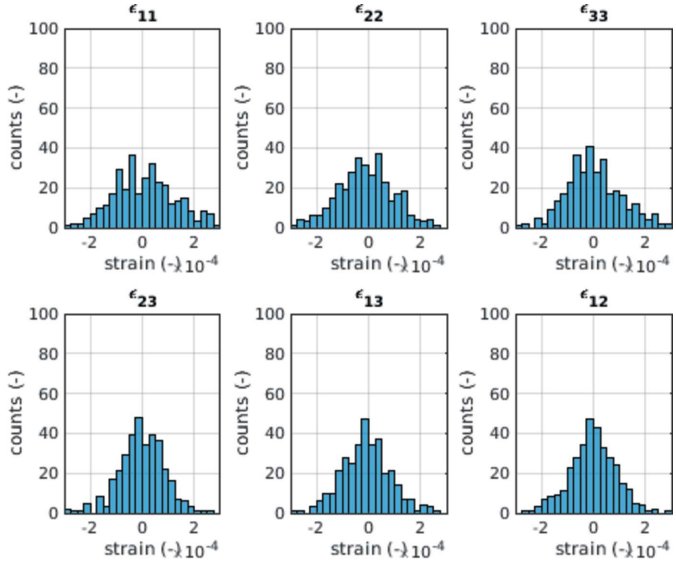

Figure 8
A histogram plot of the difference in elastic strain tensors between the tracked grains in DS-A-SS between the first scan and the scan after 500 μm intentional motion. Strain units in 10^{-4}.

Table 12
A summary of detected motions when the VOI is rotated using ξ without compensating for unintentional motion.

The last row shows the statistics after returning the VOI to its original configuration.

Motion using ξ (°)	Median misorientation (°)	Median change in COM along $\mathbf{x}_L$ (μm)	Median change in COM along $\mathbf{z}_L$ (μm)	Median change in COM along $\mathbf{y}_L$ (μm)	Number of grains matched
0.05	0.07	0	1	−6	365
0.10	0.11	0	1	−10	361
0.25	0.26	−1	0	−24	343
0.50	0.50	1	−1	−49	269
1.00	1.00	1	−2	−95	205
0.00*	0.04	1	0	0	370

MIDAS framework is accounting for the rigid-body translation appropriately.

6.3. Intentional rotations

The angular sensitivity of the instrument is characterized by intentionally rotating the sample by a known value. As described in §3, these intentional rotations can also induce unintentional motions. The unintentional motion is not compensated in DS-C-SS (§6.3.1). It is compensated in DS-C-Au (§6.3.2).

6.3.1. Stainless steel sample (DS-C-SS) without compensating for the unintentional motion. For DS-C-SS, the VOI was tipped intentionally using ξ. The VOI was *not* realigned to $\mathbf{O}_L$ after each ξ motion to investigate the effect of unintentional motion. At the end of the data acquisition, the VOI was returned to its reference configuration ($\xi = 0°$) to confirm that the motion was repeatable.

The number of grains found in the reference configuration was 379. Table 12 summarizes the result. For intentional ξ motion, the changes in $\mathbf{x}_L$ and $\mathbf{z}_L$ are negligible while the change in $\mathbf{y}_L$ increases in magnitude with increasing ξ. This indicates that the pivot point of the ξ motion and $\mathbf{O}_L$ do not coincide and an unintentional rigid-body translation is included. The number of grains matched to the grains in the reference configuration also decreases with increasing ξ. Nevertheless, the median misorientation angle for the matched grains agrees with the input ξ motion well.

The median misorientation listed in Table 11 is a convolution of the rigid-body motion introduced by the intentional motion, unintentional motion, and instrument sensitivity. If the known rigid-body rotation component is removed from the median misorientation, the resulting difference is comparable with the repeatability values presented in Table 9 even at relatively large intentional rotations. However, as described above, the intentional motion is introducing an unintentional translation in $\mathbf{y}_L$. As anticipated, the unintentional translation in $\mathbf{y}_L$ increases with the magnitude of the intentional motion.

Figure 9 shows the differences in strain as the VOI is intentionally rotated by 0.25°. Similar to the DS-A-SS case, the average component-wise strain difference is close to zero but the difference can be as large as 2×10^{-4}. Overall, the strain difference is similar to that observed in DS-A-SS.

6.3.2. Au sample (DS-C-Au) with compensation for unintentional motion. In this case, a small Au cube was measured with intentional ξ rotations. The Au cube was aligned to $\mathbf{O}_L$ after each ξ step using the radiography detector to eliminate the effect of unintentional motion. The size of the X-ray beam was 200 μm × 50 μm illuminating the Au cube (30 μm × 30 μm × 30 μm). Grain matching was trivial and did not need a radius filter. The two grains found in the original configuration was found repeatedly.

Table 13 shows that the detected misorientation is comparable with the input ξ motion. The changes in $\mathbf{x}_L$ and $\mathbf{z}_L$ are slightly larger than that detected in DS-C-SS while the change in $\mathbf{y}_L$ is significantly smaller than that in DS-C-SS. This indicates that compensation for unintentional motion worked as anticipated. The larger changes in $\mathbf{x}_L$ and $\mathbf{z}_L$ may be due to much smaller grains and slight peak smearing associated with the Au cube and need further investigation.

Similar to DS-C-SS, the median misorientation listed in Table 11 is a convolution of the rigid-body motion introduced by the the intentional motion, unintentional motion, and instrument sensitivity. If the known rigid-body rotation component is removed from the median misorientation, the

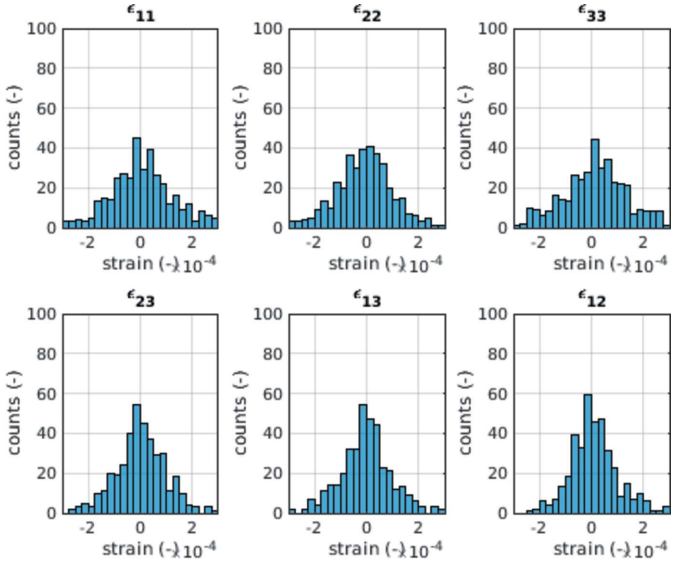

Figure 9
A histogram plot of the difference in elastic strain tensors between the tracked grains in DS-A-SS between the first scan and the scan after 0.25° intentional motion. Strain units in 10^{-4}.

Table 13
A summary of detected motions when the VOI is rotated using ξ with compensation for the unintentional motion.

Motion using ξ (°)	Mean misorientation (°)	Mean change in COM along $\mathbf{x}_L$ (μm)	Mean change in COM along $\mathbf{z}_L$ (μm)	Mean change in COM along $\mathbf{y}_L$ (μm)	Number of grains matched
0.01	0.02	−5	1	6	2
0.05	0.06	−4	−5	7	2
0.10	0.09	4	0	3	2
0.25	0.25	−7	1	4	2
0.50	0.50	−6	−6	1	2
1.00	1.00	−6	−7	0	2

Table 14
A summary of detected motions when Ω is non-zero and accounted for in the *MIDAS* analysis.

Here, the VOI is still at $\mathbf{O}_L$ but the rotation axis is no longer parallel to $\mathbf{y}_L$. The total number of grains considered is 379.

Ω (°)	Median change in COM along $\mathbf{x}_L$ (μm)	Median change in COM along $\mathbf{z}_L$ (μm)	Median change in COM along $\mathbf{y}_L$ (μm)	Median misorientation (°)	Number of grains matched
0.25	−1	−4	−4	0.06	347
0.51	4	−1	−6	0.05	315

resulting difference is small and comparable with the repeatability values presented in Table 9. Appropriately compensating for the unintentional rigid-body translation (as seen for the DS-C-SS case where a large $\mathbf{y}_L$ motion was detected) significantly reduces the magnitude of $\mathbf{y}_L$ motion nearly comparable with the numbers seen in Table 9. These results combined with those in §6.3.1 indicate that the FF-HEDM instrument is sensitive to approximately 0.05° rotation.

6.4. Intentional wedge angle (DS-D-SS)

For DS-D-SS, a set of FF-HEDM scans was conducted with non-zero Ω. This motion was realized using the three vertical motions of the optical table (Figure 1). The tilt values were acquired by the tilt sensors on the table. The three vertical motions were adjusted such that $\mathbf{y}'_L$ remains nominally on the $\mathbf{y}_L$–$\mathbf{z}_L$ plane. For each Ω motion, the VOI was positioned to $\mathbf{O}_L$ before conducting the FF-HEDM scan. During analysis of these datasets using *MIDAS*, Ω was initially set to zero and Ω was independently refined using *MIDAS* as a blind test. The values of Ω determined from *MIDAS* agreed with the actual readings from the inclinometer attached to the optical table (Figure 1). These refined values for Ω were then used to analyze the data.

Table 14 summarizes the result. As with datasets B-SS and C-SS, the number of grains found in the reference configuration was 379 and the grain radius filter was 5%. With larger magnitudes of Ω, the number of matched grains decreases. This is again due to the original VOI not being illuminated continuously during the FF-HEDM scan when Ω is non-zero. For the grains that are successfully matched, the deviation in COM and orientation are minimal indicating that the *MIDAS* framework appropriately accounts for a non-zero Ω.

When a non-zero Ω is introduced to the physical setup but not accounted for in the *MIDAS* data analysis, grain COM, orientation, and elastic strain tensor were all influenced significantly. In particular, Fig. 10 shows the component-wise elastic strain tensor distribution when Ω = 0.25° and this is not accounted for in the *MIDAS* analysis. The normal strain components deviate significantly from those measured when Ω = 0° or when Ω is accounted for. On the other hand, the shear components seem to be less affected by Ω. It is noteworthy that similar observations have been presented (Poshadel *et al.*, 2012) where some strain components are more susceptible to error than the others depending on the experimental geometry. In this case, the dominant effect of Ω is the change in sample-to-detector distance which is directly related to the normal components of strain. This highlights that appropriately accounting for Ω in the analysis is important.

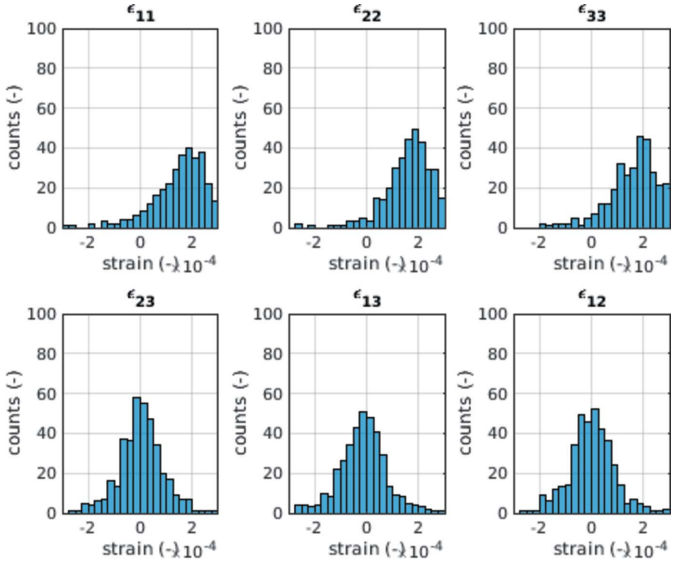

Figure 10
A histogram plot of the difference in elastic strain tensors between the tracked grains in DS-D-SS between the first scan and Ω = 0.25° without account for Ω in the *MIDAS* analysis. Strain units in 10^{-4}.

7. Discussion

7.1. Instrument performance

Based on the results presented in §6, the FF-HEDM instrument's repeatability in translation, rotation, and strain are approximately 5 μm, 0.02°, and 2×10^{-4}, respectively, when an appropriate grain matching method is used. Without an appropriate matching method, these numbers – particularly the mean and the standard deviation associated with these values – increase significantly as indicated by Tables 7 and 9. The instrument sensitivity, based on the intentional motion results (Tables 11, 12, and 13), is approximately 5 μm and 0.05° for translation and rotation, respectively. For larger grains that can take full advantage of the detector dynamic range, these values can be better.

It is worthwhile to note that the materials used in this work represent an ideal case. Both samples (stainless steel and Au cube) are fabricated from a well scattering material with well known crystal structure. They are both free of large plastic deformation. These characteristics mean that the diffraction spots do not have large angular spread and can suitably be fit with a simple peak profile function. In a real sample, subject to various types of *in situ* stimuli, the material state of constituent crystals will evolve, often increasing the defect density. This means that the diffraction spots will, in general, have large angular spread and cannot be fit well with a simple peak profile function. Since the repeatability and the sensitivity figures presented here depend on the quality of diffraction spots and how well they are fit, it is probably reasonable to anticipate that the performance figures reported here are closer to the ultimate performance attainable with the current FF-HEDM instrument. There are several avenues to improve these performance metrics. For instance, reducing the detector pixel size, ω step size used for scanning, and bandwidth of the monochromatic X-rays (Shastri, 2004) can all lead to gains in sensitivity. Currently, these approaches are often limited by available beam time or the temporal resolution required in an experiment. But significant gains in detector technology and storage ring upgrades can bring these approaches closer to reality.

As highlighted throughout this work, the stability of the physical setup and the accuracy in the representation of the setup in the analysis framework are paramount to acquiring a reliable microstructural map. As highlighted in §6.3.1 where the unintentional motion of the VOI was not compensated (DS-C-SS) physically or in §6.4 where the physical setup differed from the analysis framework (DS-D-SS), these discrepancies and instabilities can have significant consequences to the microstructural map. In DS-C-SS, many grains found in the reference configuration were lost or had large motions. In DS-D-SS, many grains seemingly had significant hydrostatic strain compared with the reference configuration. Overall, maintaining the stability of the physical setup at the level of 1 μm and 0.01° during an FF-HEDM measurement is desirable. At the APS, with the robust measurement hardware and reliable software framework to analyze the FF-HEDM data, we were able to successfully index approximately 20000 grains in a 1 mm × 1 mm × 0.1 mm VOI with 0.8 completeness. There were approximately 1.1 million diffraction spots indexed and refined by *MIDAS* running on an APS high-performance computing cluster. Figures 11 and 12 show a COM map from a VOI in a nickel-based superalloy measured using the FF-HEDM instrument and corresponding grain size distribution histogram, respectively.[18] Newer developments such as employing artificial intelligence in peak search (Liu *et al.*, 2020), addressing overlapped diffraction spots, and collaborations with larger high-performance computing facilities like the Argonne Leadership Computing Facility (Wozniak *et al.*, 2015; Wolf, 2014) will push this limit further and allow us to provide grain-resolved information in polycrystalline materials with a higher degree of structural complexity than ones HEDM can investigate today. This stability requirement will be even more stringent as the technique is pushed to investigate more complex material systems.

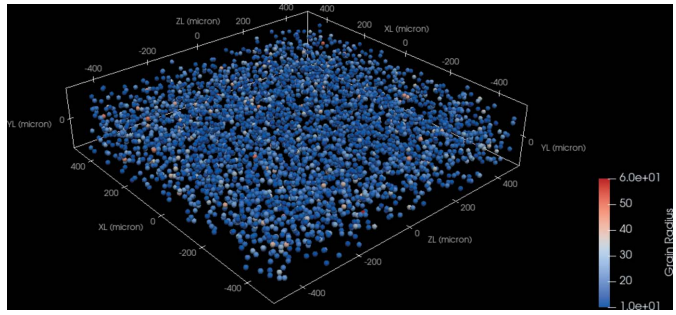

Figure 11
An example of a grain COM map acquired using the FF-HEDM instrument. The number of grains found is approximately 20000. The position of the dots denotes the grain COM in space and the color of the dots denotes the grain radius.

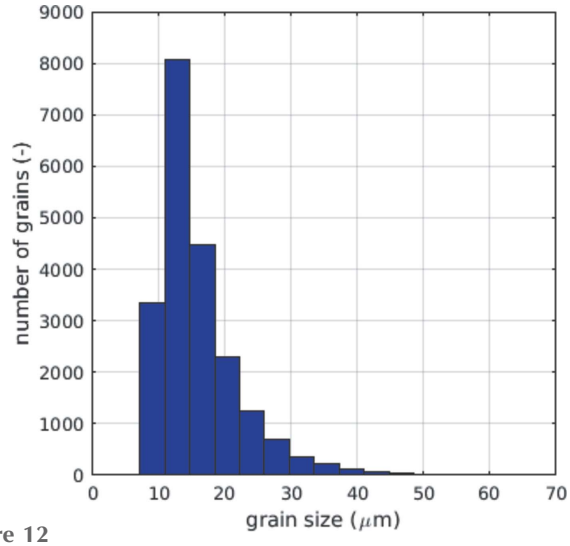

Figure 12
The grain size distribution based on the FF-HEDM map in Fig. 11.

[18] The incident beam size was 1.7 mm along $\mathbf{x}_L$ and 0.2 mm along $\mathbf{y}_L$. The sample cross-section was 1 mm × 1 mm. With appropriate data acquisition and analysis settings, the full dynamic range of the detector could be utilized to obtain a grain map of a polycrystalline aggregate where the larger grains are approximately six times the smaller ones.

7.2. Inconsistency between the datasets

While the FF-HEDM instrument performs reasonably well during a measurement session, there are also inconsistencies between the datasets acquired at different times that highlight the limitations of FF-HEDM and warrants further investigation. The number of grains found in DS-A-SS is significantly smaller than those found in DS-B-SS, DS-C-SS, and DS-D-SS even though the identical sample was illuminated in all four datasets. The number of grains found in DS-A-SS was approximately 200 while the number of grains found in DS-B-SS, DS-C-SS, and DS-D-SS was approximately 380. However, the beam size used for DS-A-SS was twice as large as that used for DS-B-SS, DS-C-SS, and DS-D-SS. Given the beam size, the number of grains found in these datasets should show an opposite trend. However, if we considered the size of the illuminated volume and the number of grains found to compute the average grain radii (assuming the grains are spherical) in DS-A-SS and the other SS datasets, the grain radius is approximately 60 µm and 40 µm for DS-A-SS and the other SS datasets, respectively. A grain radius range of 40–60 µm is reasonable for this material based on metallography.

The discrepancy in the number of grains found between different datasets is most likely because of the reflections used in the analysis (Table 3). In the case of DS-A-SS and associated *MIDAS* analysis, many reflections with vastly different scattering power were used while a smaller number of reflections with higher scattering power were used in other datasets. Satisfying the completeness value of 0.8 in DS-A-SS, therefore, is probably more challenging than the other datasets. This implies that the exposure settings for data acquisition and the choice of reflections used in the analysis can influence the resulting microstructure map.

In the case of DS-A-SS, it is noteworthy that there are a significant number of diffraction spots that are not assigned or indexed to grains. The average N_{grain} in DS-A-SS is 214 and the anticipated number of diffraction spots for a grain is 244 (Table 3); this means that 52216 diffraction spots and 41773 diffraction spots need to be detected with a completeness of 1 and 0.8, respectively. When these are compared with the actual number of diffraction spots detected, approximately 50% of the detected diffraction spots are not assigned to grains. Figure 13 shows a histogram of the assigned (and indexed to grains) and unassigned diffraction spots in a DS-A-SS scan. This figure indicates that the intensity of the unassigned diffraction spots is typically lower compared with that for the assigned diffraction spots. Dissecting Fig. 13 further into different {*hkl*}s, we can see that the majority of the inner and generally more intense diffraction spots are unassigned (Fig. 14) while the majority of the outer and generally less intense spots are assigned to grains (Fig. 15). A combination of high completeness and inclusion of higher-order diffraction spots in the *MIDAS* analysis are contributing factors to a large number of detected diffraction spots being unassigned to grains. This implies that a grain detection limit associated with the grain size distribution in the VOI exists and highlights that an FF-HEDM experiment and associated data analysis need

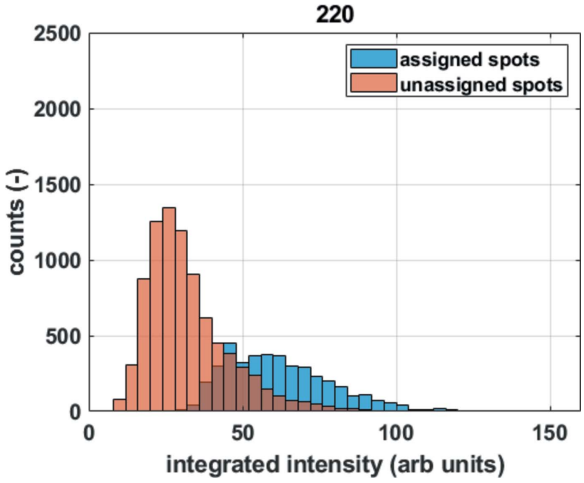

Figure 14
A histogram of the number of diffraction spots that are assigned or unassigned to grains in a DS-A-SS scan for the {220} ring.

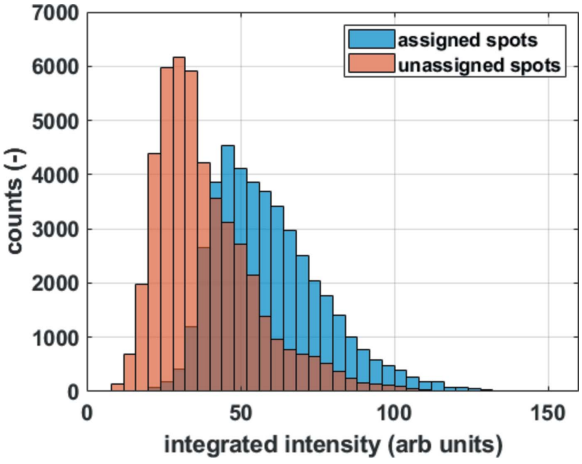

Figure 13
A histogram of the number of diffraction spots that are assigned or unassigned to grains in a DS-A-SS scan.

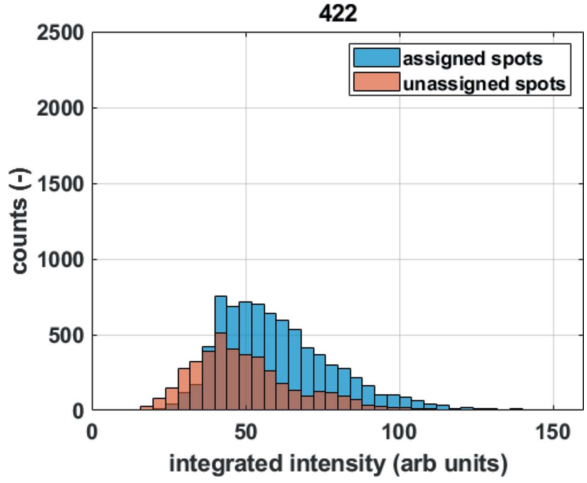

Figure 15
A histogram of the number of diffraction spots that are assigned or unassigned to grains in a DS-A-SS scan for the {422} ring.

to be designed and conducted carefully, particularly when the goal for acquiring a 3D grain-resolved microstructural map is to investigate rare-event driven phenomena in materials. An independent measurement like optical or electron microscopy to confirm the FF-HEDM results (at least statistically) is encouraged, particularly when investigating a new or unknown material.

As described in §4, the analysis parameters for each dataset presented in this work were carefully determined to yield stable and reproducible results at the time the measurements were conducted. The number of grains found in DS-A-SS can be increased to more than 500 grains if the number of reflections used in the analysis decreased, completeness threshold decreased, or peak detection threshold altered. However, adjusting these analysis parameters to ensure that all SS datasets have a consistent number of grains matching the illuminated volume size will be misleading. More importantly, we are currently working with the 3D EBSD community to understand the effects of *MIDAS* analysis parameters on the resulting microstructure better and we hope to report on this in the near future.

7.3. Matching grains

In situ grain-resolved X-ray microscopy, including the FF-HEDM technique described here, has been lauded as a novel non-destructive characterization technique capable of investigating the small changes that occur at the grain length scale while applying macroscopic stimuli. This implies that matching of grains measured at different macroscopic stimuli levels needs to be robust and reliable. As we investigate more complex material systems with smaller grain sizes, grain matching will be more challenging. There are several methods in *MIDAS* and associated tools to enhance the reliability and robustness of grain matching and they are listed here:

(i) The diffraction data acquired with applied macroscopic stimulus can be analyzed with the grains found at the reference state as the initial guess to instantiate the indexing process. In this case, *MIDAS* will only look for grains that existed in the reference state. Whether the grains found in the reference state are indexed again needs to be verified. Additionally, the number of spots that are unclaimed also needs to be monitored.

(ii) If the list of grains found in the reference state is not used to instantiate the indexing process, various grain matching methods can be used. In this work, the grains were matched by considering the entire misorientation and distance tables computed between two sets of grains measured in between an intentional motion. Additional grain matching filters such as grain size can also be use for grain matching.

Another important aspect of grain matching and operating on the microstructure maps is accounting for the sample frame. In this work, the relationship between the sample frame and the laboratory frame was not monitored diligently because the sample frame is not highly relevant. However, when a 'real' sample with a very specific frame is measured, the relationship between the sample frame and the laboratory frame needs to be tracked. After all, reporting the orientation relationship between the crystal and the laboratory frame is not the goal of HEDM; the goal is to report the orientation relationship between the crystal and the sample frame. Therefore, appropriate fiducial markers and methodologies to extract the relationship between the sample and laboratory frames is crucial for HEDM measurements. At the APS 1-ID-E, complementary tomography measurements are routinely conducted to assist in monitoring the relationship between the sample and the laboratory frames. Furthermore, various types of fiducial markers (Shade *et al.*, 2016) can be attached near the VOI so that a sample can be removed from the beamline to evolve its state before measuring it again with HEDM for processes that are not suitable or unavailable for *in situ* experiments.

8. Summary and outlook

Microscopy techniques using high-energy X-rays are becoming more accessible to the general users of synchrotron light sources. These techniques are capable of providing complementary information that conventional characterization techniques often cannot provide. It is important for the general users to understand the capabilities of these techniques. In this work, we demonstrated the performance of the FF-HEDM instrument at the APS 1-ID-E endstation. When an appropriate grain matching method is used, the FF-HEDM instrument's repeatability is approximately 5 µm in translation, 0.02° in rotation, and 2×10^{-4} in strain; the instrument sensitivity is approximately 5 µm in translation and 0.05° in rotation. As the FF-HEDM technique relies on acquiring the diffraction spots, the performance values presented here can be better for the larger grains that can take full advantage of the detector dynamic range. The instrumental performance needs to be considered carefully when interpreting an FF-HEDM map.

In addition to describing the FF-HEDM instrument at the APS, this work illustrates a methodology that can be used for cross-instrument comparison and benchmarking studies. As different variants of grain-resolved non-destructive techniques come on-line, it is important and timely that the diffraction microscopy and imaging community organize comprehensive tests to characterize the instruments' sensitivity and performance by investigating a common VOI from a round-robin sample. Cross-checking the microstructure maps from different grain-resolved non-destructive and destructive techniques will be important to understand the strengths and challenges associated with these techniques. In our work, radiography or tomography was used to ensure that the same VOI is illuminated between intentional motions. In addition to tomography, a set of fiducial markers to track the orientation of the VOI with respect to the physical setup will be important for conducting these cross-checking exercises.

The FF-HEDM datasets collected for this work will be available to the community at the Materials Data Facility (Blaiszik *et al.*, 2016) for software development and round-robin software tests. Such tests will be helpful in improving

various software frameworks and bringing consistency between results produced by these frameworks.

Acknowledgements

This research supported by Argonne National Laboratory and used resources of the Advanced Photon Source, a US Department of Energy (DOE) Office of Science User Facility operated for the DOE Office of Science by Argonne National Laboratory (Contract No. DE-AC02-06CH11357). The authors would like to thank Jon Almer, Ali Mashayekhi, and Rogelio Ranay of the APS. The authors would like to thank Aaron Stebner of Colorado School of Mines for providing the sample used in this work. The authors would like to thank Paul Shade of the US Air Force Research Laboratory for fabricating the gold cube sample and providing the nickel-based superalloy sample.

Funding information

Funding for this research was provided by: US Department of Energy, Office of Science (contract No. DE-AC02-06CH11357).

References

Beaudoin, A., Obstalecki, M., Tayon, W., Hernquist, M., Mudrock, R., Kenesei, P. & Lienert, U. (2013). *Acta Mater.* **61**, 3456–3464.

Bernier, J. V., Barton, N. R., Lienert, U. & Miller, M. P. (2011). *J. Strain Anal. Eng. Des.* **46**, 527–547.

Bernier, J. V., Suter, R. M., Rollett, A. D. & Almer, J. D. (2020). *Annu. Rev. Mater. Res.* **50**, 395–436.

Blaiszik, B., Chard, K., Pruyne, J., Ananthakrishnan, R., Tuecke, S. & Foster, I. (2016). *JOM*, **68**, 2045–2052.

Blaiszik, B., Ward, L., Schwarting, M., Gaff, J., Chard, R., Pike, D., Chard, K. & Foster, I. (2019). *MRS Commun.* **9**, 1125–1133.

Borbély, A., Renversade, L. & Kenesei, P. (2014*a*). *J. Appl. Cryst.* **47**, 1585–1595.

Borbely, A., Renversade, L., Kenesei, P. & Wright, J. (2014*b*). *J. Appl. Cryst.* **47**, 1042–1053.

Fenner, R. (2021). *The APS upgrade: building a brighter future*, https://www.aps.anl.gov/APS-Upgrade.

Freiman, S. W. (2001). Standard Reference Material 1990. National Institute of Standards and Technology, Gaithersburg, MD, USA.

Freiman, S. W. & Trahey, N. M. (2000). NIST Standard Reference Material 660a. National Institute of Standards and Technology. National Institute of Standards and Technology, Gaithersburg, MD, USA.

Gill, A. S., Zhou, Z., Lienert, U., Almer, J., Lahrman, D. F., Mannava, S. R., Qian, D. & Vasudevan, V. K. (2012). *J. Appl. Phys.* **111**, 084904.

Gotz, A., Dale, D., Knudsen, E. B., Suchet, G., Vaughan, G., Sorensen, H. O., Oddershede, J., Wright, J., Kieffer, J., Majkut, M., Schmidt, S., Huizenga, R., Foulis, D. L., Gerring, M., Bernier, J., Evans, K., Paithankar, K. & Elhachi, Y. (2003). *fable*, https://sourceforge.net/projects/fable/.

Ivanyushenkov, Y., Harkay, K., Borland, M., Dejus, R., Dooling, J., Doose, C., Emery, L., Fuerst, J., Gagliano, J., Hasse, Q., Kasa, M., Kenesei, P., Sajaev, V., Schroeder, K., Sereno, N., Shastri, S., Shiroyanagi, Y., Skiadopoulos, D., Smith, M., Sun, X., Trakhtenberg, E., Xiao, A., Zholents, A. & Gluskin, E. (2017). *Phys. Rev. Accel. Beams*, **20**, 100701.

Kaiser, D. L. & R. L. Watters, J. (2007). NIST Standard Reference Material 674b. National Institute of Standards and Technology, Gaithersburg, MD, USA

Kyrieleis, A., Ibison, M., Titarenko, V. & Withers, P. (2009). *Nucl. Instrum. Methods Phys. Res. A*, **607**, 677–684.

Larson, B., Yang, W., Tischler, J., Ice, G., Budai, J., Liu, W. & Weiland, H. (2004). *Int. J. Plast.* **20**, 543–560.

Lee, J., Almer, J., Aydıner, C., Bernier, J., Chapman, K., Chupas, P., Haeffner, D., Kump, K., Lee, P., Lienert, U., Miceli, A. & Vera, G. (2007). *Nucl. Instrum. Methods Phys. Res. A*, **582**, 182–184.

Lee, J. H., Aydıner, C. C., Almer, J., Bernier, J., Chapman, K. W., Chupas, P. J., Haeffner, D., Kump, K., Lee, P. L., Lienert, U., Miceli, A. & Vera, G. (2008). *J. Synchrotron Rad.* **15**, 477–488.

Lienert, U., Li, S. F., Hefferan, C. M., Lind, J., Suter, R. M., Bernier, J. V., Barton, N. R., Brandes, M. C., Mills, M. J., Miller, M. P., Jakobsen, B. & Pantleon, W. (2011). *JOM*, **63**, 70–77.

Liu, Z., Sharma, H., Park, J. S., Kenesei, P., Almer, J., Kettimuthu, R. & Foster, I. (2020). *BraggNN: Fast X-ray bragg peak analysis using deep learning*, http://arxiv.org/abs/2008.08198.

Ludwig, W., King, A., Reischig, P., Herbig, M., Lauridsen, E., Schmidt, S., Proudhon, H., Forest, S., Cloetens, P., Roscoat, S. R., Buffière, J., Marrow, T. & Poulsen, H. (2009). *Mater. Sci. Eng. A*, **524**, 69–76.

Park, J. S., Lienert, U., Dawson, P. R. & Miller, M. P. (2013). *Exp. Mech.* **53**, 1491–1507.

Park, J.-S., Zhang, X., Sharma, H., Kenesei, P., Hoelzer, D., Li, M. & Almer, J. (2015). *J. Mater. Res.* **30**, 1380–1391.

Poshadel, A., Dawson, P. & Johnson, G. (2012). *J. Synchrotron Rad.* **19**, 237–244.

Poulsen, H. F. (2004). *Three-Dimensional X-ray Diffraction Microscopy*, Vol. 205 of *Springer Tracts in Modern Physics*. Springer-Verlag.

Poulsen, H. F., Nielsen, S. F., Lauridsen, E. M., Schmidt, S., Suter, R. M., Lienert, U., Margulies, L., Lorentzen, T. & Juul Jensen, D. (2001). *J. Appl. Cryst.* **34**, 751–756.

Sagoff, J. (2020). *High-throughput x-ray diffraction instrument comes to Argonne's Advanced Photon Source*, https://www.anl.gov/article/highthroughput-xray-diffraction-instrument-comes-to-argonnes-advanced-photon-source.

Said, A. H. & Shastri, S. D. (2010). *J. Synchrotron Rad.* **17**, 425–427.

Schmidt, S. (2014). *J. Appl. Cryst.* **47**, 276–284.

Shade, P. A., Menasche, D. B., Bernier, J. V., Kenesei, P., Park, J.-S., Suter, R. M., Schuren, J. C. & Turner, T. J. (2016). *J. Appl. Cryst.* **49**, 700–704.

Sharma, H. (2020). *Microstructure Identification Using Diffraction Analysis Software (MIDAS)*, https://github.com/marinerhemant/MIDAS.git.

Sharma, H. (2021). In preparation.

Sharma, H., Huizenga, R. M. & Offerman, S. E. (2012*a*). *J. Appl. Cryst.* **45**, 693–704.

Sharma, H., Huizenga, R. M. & Offerman, S. E. (2012*b*). *J. Appl. Cryst.* **45**, 705–718.

Shastri, S. D. (2004). *J. Synchrotron Rad.* **11**, 150–156.

Shastri, S. D., Fezzaa, K., Mashayekhi, A., Lee, W.-K., Fernandez, P. B. & Lee, P. L. (2002). *J. Synchrotron Rad.* **9**, 317–322.

Shastri, S. D., Kenesei, P., Mashayekhi, A. & Shade, P. A. (2020). *J. Synchrotron Rad.* **27**, 590–598.

Suter, R. M., Hennessy, D., Xiao, C. & Lienert, U. (2006). *Rev. Sci. Instrum.* **77**, 123905.

Thompson, A. C., Attwood, D. T., Gullikson, E. M., Howells, M. R., Kortright, J. B., Robinson, A. L., Underwood, J. H., Kim, K.-J., Kirz, J., Lindau, I., Pianetta, P., Winick, H., Williams, G. P. & Scofield, J. H. (1985). *X-ray Data Booklet*. Center for X-ray Optics, Lawrence Berkeley National Laboratory, Berkeley, CA, USA.

Wolf, L. (2014). *ALCF HEDM*, https://www.alcf.anl.gov/news/boosting-beamline-performance.

Wozniak, J. M., Sharma, H., Armstrong, T. G., Wilde, M., Almer, J. D. & Foster, I. (2015). *Proceedings of the 2014 IEEE/ACM International Symposium on Big Data Computing (BDC 2014)*, pp. 26–34. Institute of Electrical & Electronics Engineers.